

# 3D statistical neuroanatomical models from 305 MRI volumes

A C Evans, D L Collins, S R Mills<sup>†</sup>, E D Brown<sup>†</sup>, R L Kelly<sup>†</sup>, T M Peters  
Montreal Neurological Institute and McGill University  
3801 University St, Montreal QC, Canada. H3A-2B4  
and  
Science Applications International Corporation<sup>‡</sup>  
10260 Campus Pt. Drive,  
San Diego, California, CA 92121

## I. INTRODUCTION

Recently, there has been a rapid growth in the use of 3D multi-modal correlative imaging for studies of the human brain. Such techniques have found applications in the areas of (i) disease diagnosis, (ii) longitudinal monitoring of disease progress or remission, (iii) pre-operative evaluation and surgery planning, (iv) functional neuroanatomy of sensorimotor and cognitive processes and (v) morphometric analysis of neuroanatomical variability among normal brains. Many of these domains are methodological components of the developing field of brain mapping which seeks to identify functional systems subserving cognitive and sensorimotor processes in the human brain. In most brain-mapping studies, cerebral blood flow (CBF) is measured by PET or functional MRI scanning in a baseline state and during some form of cerebral activation, e.g. sensorimotor stimulus or cognitive task. Regional CBF changes indicate brain areas involved in stimulus processing. These focal changes are often too small ( $\leq 10\%$ ) to be discerned from a single subject and the experiment is repeated in a series of individuals. The results are averaged after linear re-sampling of each data volume data into a standardized or stereotaxic 3D coordinate space to remove gross differences in brain dimensions and orientation [5,6]. Limitations arise from non-linear neuroanatomic variation persisting after linear re-sampling [7]. These differences prevent exact superposition of equivalent activation sites from different subjects, thereby reducing the signal-to-noise gain. To investigate the extent of this residual variability we have collected over 300 MRI volumetric datasets from normal individuals and transformed these datasets into stereotaxic space using a 3D linear re-sampling algorithm. We then generated a series of statistical measures which express this population non-linear variability in the form of parametric volumes e.g. mean intensity, intensity variance. A model for anatomical variability, expressed as the width of a Gaussian blurring kernel applied to an ideal single subject, was developed and tested against the observed data.

<sup>†</sup>This work was supported by grants from the Medical Research Council of Canada

## II. DATA ACQUISITION

At the Montreal Neurological Institute a database of MRI volumes has been obtained from 305 young, normal right-handed subjects (239 males ; 66 females ; age 23.4  $\pm$  4.1). All MRI studies were performed on a Philips Gyroscan 1.5 Tesla superconducting magnet system. Using 3D spin-echo acquisition, 64 non-overlapped T<sub>1</sub>-weighted (T<sub>R</sub>=400msec, T<sub>E</sub>=30msec) image planes are collected at 2 mm intervals over the whole brain. Measurements of the dimensions of an MRI calibration phantom indicate negligible geometric distortion through the central portion of the MRI imaging field.

## III. 3D IMAGE-MATCHING PROCEDURE

We have implemented a 3D feature-matching procedure which employs repetitive evaluation of the feature cross-correlation function (FCCF) between two images [1-3]. The required transformation is found using the SIMPLEX optimization algorithm on 9 linear parameters (3 translations, 3 rotations and 3 scales). The feature-matching procedure operates in a multi-scale loop, beginning with a heavily-smoothed version of each image and successively sharpening the images at each iteration. The use of blurred images for obtaining approximate transformation parameters reduces the likelihood of encountering local minima during the search and is approximately 4 times faster than single-stage high-resolution optimization. At each stage the original image is first convolved with a 3D Gaussian smoothing kernel before the best transformation is determined by maximizing the FCCF at scales (SD of Gaussian kernel) of 16, 8 and 4mm. At present, the method uses image intensity and gradient magnitude as features. For the linear mapping approach employed in this work, recovering a known transformation applied to a given MRI volume (intra-subject) exhibits r.m.s. errors for rotation, translation and landmark distance were less than or equal to 0.1°, 0.1mm and 0.2mm respectively. Inter-subject registration residuals can be estimated by identifying corresponding

landmarks in different volumes. We have previously shown an r.m.s distance of 6.65mm between equivalent landmarks from different individuals [3].

#### IV. STEREOTAXIC TRANSFORMATION

For comparison of individual MRI volumes we employed a modification of the stereotaxic space of Talairach and Tournoux (1988) in a two-stage process. The cross-correlation procedure requires a starting target volume. This was generated manually as follows. A set of neuroanatomical landmarks were manually identified in each volume which defined an origin (the anterior commissure(AC), located on the brain mid-line), a base plane passing through both the AC and the posterior commissure (PC), and three orthogonal axes extending to the edge of the brain within (X,Y) and perpendicular (Z) to the AC-PC plane. Equivalent coordinates identified in the stereotaxic space defined the 9 parameter linear transformation. The transformed volumes were re-sampled, using tri-cubic interpolation, to a 256 x 256 x 160 raster with voxel dimensions of 0.67mm x 0.86mm x 0.75mm. Application of this re-sampling to each of the 305 MRI volumes, normalization for constant mean signal intensity in each transformed volume and intensity-averaging yielded a mean MRI volume [6,7]. Secondly, each individual volume, in its original orientation, was again transformed into stereotaxic space, this time using the average MRI volume from stage one as a target volume for the automatic 3D cross-correlation procedure described above. This reduced the impact of subjectivity in choice of landmarks during the first stage and resulted in a sharpened average MRI volume.

#### V. CORRECTION FOR R.F. INHOMOGENEITY

The MRI database is contaminated by a small radiofrequency inhomogeneity due to the linearly polarized 2-coil design of the MRI imaging unit. The inhomogeneity appears as a band of elevated image intensities that runs from the lower left to the upper right corner of each transverse slice in the 3D MRI volume. It causes an intensity imbalance of up to 3% between mirror image points in the left and right hemispheres of the brain image, and is particularly troublesome for the interpretation of left/right asymmetries in the image. Since the artifact is a low frequency phenomenon, we parameterized this inhomogeneity in the mean brain image and used the resulting fitted intensity surface to remove the inhomogeneity from members of the brain image database used in subsequent analysis. The inhomogeneity was parameterized as a multiplicative quadratic that is invariant along a 45° line extending from (0,0) to (256,256) pixels in each transverse slice of the native data volume. This geometry is an idealization corresponding to a subject head whose z-axis is

aligned with the axis of the coils. In stereotaxic space the axis of the quadratic is at 38° to the x-axis due to the change in sample spacing in the x and y directions. The parametrization contains two adjustable parameters which control the relative amplitude modulation of the inhomogeneity, a, and the vertical offset of the axis from the origin, b. The parametrization used is the following, with x and y in pixel coordinates for 256 by 256 transverse slices with (0,0) in the lower left corner.

$$f(x,y,z) = a.(-x.\sin(t)+(y-b).\cos(t))^2+1 ; t=38^\circ$$

The parameters a and b were determined by performing a chi-squared fit to a hemispherical data volume formed by dividing the left half of the mean brain by the right half (L/R image). This L/R image removes much of the natural anatomical brain variation, which is close to being left/right symmetric, and accentuates the inhomogeneity. The fitting function for the L/R image is  $f(xL,y,z)/f(xR,y,z)$  where xL and xR are mirror symmetric values of x. Inverse variance weight functions were required at each voxel in the L/R volume for the chi-squared fit, and these weights were determined from the voxel variance map associated with the mean brain using standard linear error propagation for the quotient form of the L/R data.

#### VI. CONSTRUCTION OF ANATOMICAL BLURRING KERNEL

The mean brain constructed from the registered MNI image database has the appearance of a blurred individual brain image. We constructed an empirical blurring kernel which, when applied to an individual brain, results in a blurring similar to that which occurs in the mean brain. To remove the impact of noise in the individual data, smoother characterizations were obtained of the Fourier transform of a typical individual brain,  $B(k)$ , and the mean brain,  $A(k)$ . We found that these Fourier transforms were decidedly non-Gaussian. After experimentation with alternate forms, we have found that the absolute value of both  $A(k)$  and  $B(k)$  can be adequately parametrized as the exponential of a Gaussian form,

$$|A(k)| = C_a.\exp(Ga(k))$$

$$G_a(k) = D_a.\exp(-(\frac{kx}{dx_a})^2 - (\frac{ky}{dy_a})^2 - (\frac{kz}{dz_a})^2)$$

and similarly for  $|B(k)|$ . The adjustable parameters  $C_a, D_a, dx_a, dy_a,$  and  $dz_a$  were determined by a chi-squared fit to the absolute value of the mean brain image Fourier transform over a band of k-values that excludes the lowest frequencies (less than 0.1 cycle/mm) and highest frequencies (greater than 80% of Nyquist) included in the discrete Fourier transform. The low frequencies were excluded because they correspond to large scale image structure which is not affected by the inter-subject anatomical blurring be-

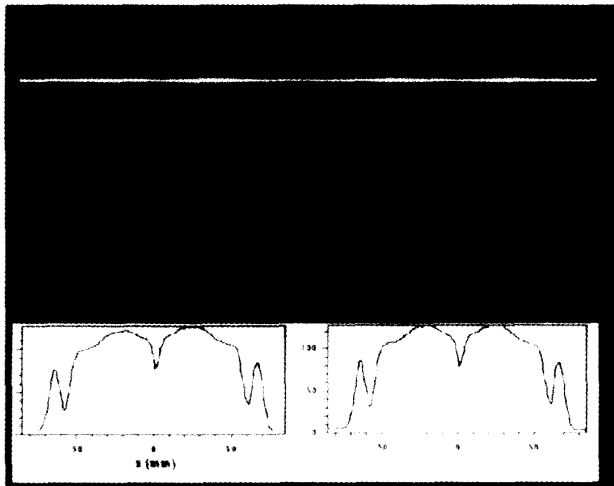


Figure 1: Effect of r.f. inhomogeneity correction

ing characterized. The high frequency region was excluded because we observe empirically that the Fourier transforms stopped rolling off and hit a white noise floor at about 80% of Nyquist. Similarly,  $C_b$ ,  $D_b$ ,  $dx_b$ ,  $dy_b$ , and  $dz_b$  were determined separately for each individual brain. The blurring hypothesis requires that  $B(k)$  and  $A(k)$  are linearly related by a kernel  $K(k) = A(k)/B(k)$ . When  $K(k)$  is applied to the Fourier transform of an individual brain,  $I(k)$ , the resultant  $k$ -space distribution,  $K(k).I(k)$ , corresponds to a real space image volume which is a blurred version of the original individual image. When the inverse of  $K(k)$  is applied to the Fourier transform of the mean brain,  $M(k)$ , the resultant  $k$ -space distribution,  $M(k)/K(k)$ , corresponds to a sharpened version of the mean brain.

## VII. RESULTS

**Correction for R.F. inhomogeneity:** The parameters derived for the quadratic model of r.f. inhomogeneity were  $a = -9.09E-06$  and  $b = 11.7$ . Results are shown in Figure 1 which compares 2D and 1D transverse mean image slices before and after removal of the inhomogeneity. The 1D slices in particular show the scale of the small inhomogeneity modulation in the contaminated mean brain and its absence after removal of the inhomogeneity.

**Variance image:** Figure 2 shows a single slice through the volume of variance in normalized MRI intensity. Regions of high variance are evident near sharp boundaries in MRI intensity such as the ventricular margins. Low variance is exhibited in the white matter regions and intermediate variance is observed in cortex, being highest in the perisylvian regions.

**Construction of Anatomical Blurring Kernel:** The parameters determined by this fitting procedure fall into two classes. The fitted values of each of the param-



Figure 2: Variance of normalized MRI intensity over 305 stereotaxic MRI volumes

eters for individual brains were found to cluster together in a range of values that is quite distinct from the value of the corresponding parameter for the mean brain as shown in Table I. The width parameters are smaller in the mean brain, as expected. Figure 3 illustrates a 1D cut through the 3D FFT of the mean MRI volume and a single MRI volume. Also shown is a composite fit to the individual brain derived by taking the mean value for the parameters  $C_b$ ,  $D_b$ ,  $dx_b$ ,  $dy_b$ , and  $dz_b$ .

The blurring kernel was constructed by using the mean values of the parameter clusters for  $B(k)$  and the fitted values from the mean brain for  $A(k)$ . To avoid spurious high frequency effects associated with frequencies outside the fitting region we applied a cosine taper to  $B(k)/A(k)$  with a rolloff to 0.5 at 80% of Nyquist. 1D axial cuts through the resulting 3D  $k$ -space blurring kernel are shown in Figure 4, and axial cuts through the corresponding real space blurring kernel are shown in Figure 5 (displayed with the actual asymmetric sampling of the registered brain image database). Owing to the non-Gaussian nature and the inadequate z-sampling of the real space form of the kernel, the effective width in each dimension of the kernel was determined by inverse Fourier transformation of the second moment of the frequency kernel. These figures were then used to generate an effective FWHM for the real space kernel as shown in Table II.

Figure 6 is a visual display of the effects of the blurring kernel and its inverse on mean and individual brain image volumes. The upper left quadrant is a transverse slice of the mean brain volume, and the upper right quadrant is the same slice from the sharpened version of the mean volume obtained by application of the inverse blurring kernel. These images are to be compared with the slices of an individual image volume directly below them. The lower right quadrant is the corresponding slice of an individual

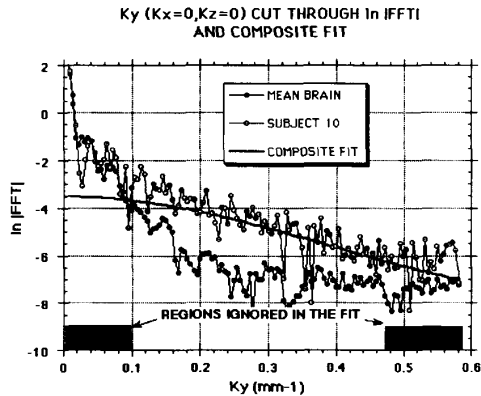


Figure 3: 1D cuts in Y-direction through the  $\ln$ -FFT-transforms of mean MRI and a single MRI. Also shown is the average fit to an individual MRI, derived from individual fit parameters of Table I

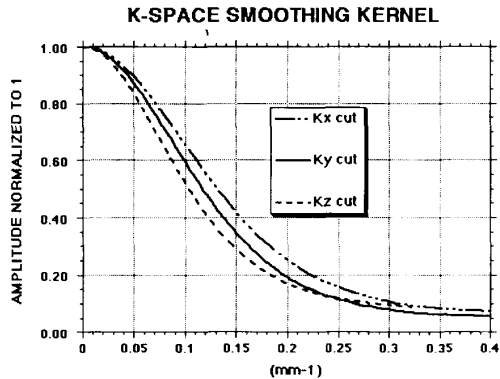


Figure 4: 1D cuts through blurring kernel, frequency domain

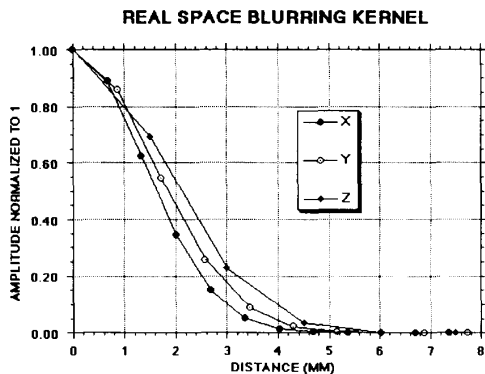


Figure 5: 1D cuts through blurring kernel, real domain

TABLE I  
Width parameters ( $mm^{-1}$ ) obtained from mean MRI volume and from  $N=50$  individual MRI volumes.

Fit parameter	Mean $\pm$ SD
$dx_a$	$0.207 \pm 0.000$
$dy_a$	$0.188 \pm 0.000$
$dz_a$	$0.148 \pm 0.000$
$dx_b$	$0.414 \pm 0.017$
$dy_b$	$0.390 \pm 0.019$
$dz_b$	$0.233 \pm 0.012$

TABLE II  
R.m.s. width (mm) in each dimension and effective FWHM (mm) of blurring kernel

Distance Measure	Width
$\sigma_x = \sqrt{\langle x^2 \rangle}$	1.52
$\sigma_y = \sqrt{\langle y^2 \rangle}$	1.70
$\sigma_z = \sqrt{\langle z^2 \rangle}$	1.97
FWHM = $2.35\sqrt{\langle x^2 \rangle + \langle y^2 \rangle + \langle z^2 \rangle}/3$	4.09

brain volume from the registered dataset, and the lower left quadrant is the same slice after the individual volume has been subjected to the blurring kernel.

## VIII. DISCUSSION

Despite the loss in resolution for the highly variable secondary cortical features, the average MRI atlas provides a remarkable amount of detail on the most probable position of major features, e.g. the central sulcus, parieto-occipital sulcus, calcarine sulcus. In the deeper brain, close to the transformation origin, some details are evident which are difficult to distinguish in single images e.g. the dorsomedial nucleus of the thalamus. White matter tracts are apparent as slightly darker projections than the adjacent white matter e.g. optic radiations. The MRI intensity variance image exhibited sharp increases at edge regions, e.g. ventricular borders, where intensity changes rapidly. In such regions, the width of the variance map for normalized MRI intensity is a useful indicator of local spatial variation in the corresponding anatomical boundary. However it does not provide useful information in areas where adjacent regions have similar contrast. The blurring kernel obtained by taking the average ratio of  $A(k)/B(k)$  over a population of MRI volumes has an effective FWHM of 4.08mm (Table I). Figure 6 shows the effect of this kernel on a single MRI volume and, when applied in the inverse direction, on the mean MRI volume. While this latter operation cannot restore the highest spatial frequencies where noise is

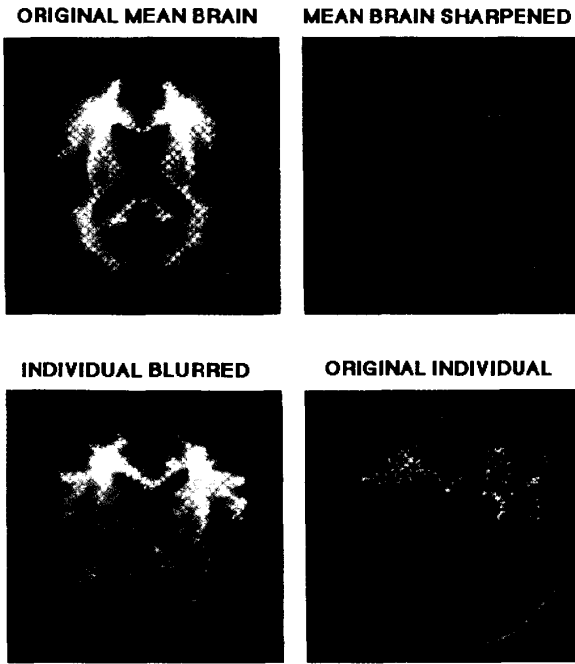


Figure 6: Effect of blurring kernel on individual images. Bottom images are from a representative individual brain.

limiting, it raises the possibility of identifying an 'ideal' individual whose MRI volume has the highest intensity correspondence with the sharpened mean MRI. In previous work [3,5] we found a 3D r.m.s. distance ( $\sigma_r$ ) between corresponding landmarks of 6-7mm. For an isotropic 3D Gaussian distribution this would correspond to a  $\sigma_x$  of 3.5-4.0mm and a FWHM ( $2.35\sigma_x$ ) of 8.2-9.4mm. This FWHM discrepancy of a factor of approximately two between this study and previous landmark-based results may be explained by the different methodologies and assumptions employed. Previous studies included numerous manually-identified cortical landmarks where 3D spatial variations of up to 5cm are possible. The current automated method, based on normalized MRI intensity and assuming a single spatially invariant blurring kernel, cannot model such gross deformation adequately, particularly in regions with highly variable and complicated folding patterns. The method is weighted toward regions with sharper intensity edges such as those around deep brain structures, e.g. basal ganglia and ventricular margins. It will also detect radial shifts at the cortical margin but not tangential shifts unless they correspond to radially-oriented sulci being moved tangentially. These will lead to a systematic underestimation of the overall deformation. For complete mapping of neuroanatomical variability, the MRI intensity for each voxel in each MRI volume must be replaced by an anatomical label and a probability assigned for each voxel having a particular label. This requires a precise segmentation

of each MRI volume into component structures, features and tissue types. Manual labelling, in addition to being prohibitively time-consuming, would introduce intra- and inter-observer variations in labelling strategy which would confound the overall goal. Completely automatic and accurate image segmentation at the regional level is as yet an unsolved problem. At the MNI, three overlapping projects are addressing the problem of anatomical variability, aiming to obtain the automatic labelling of 3D MRI datasets by tissue-type [8], by specific neuroanatomical volume [1,2] and by gyral/sulcal surface anatomy [9].

#### REFERENCES

- [ 1 ] Collins D.L., Dai W., Peters T.M., Evans A.C. *Model-based segmentation of individual brain structures from MRI data Visualization in Biomedical Computing 1992, Proc SPIE 1808* : 10-23 ; 1992a
- [ 2 ] Collins D.L., Peters T.M., Evans A.C. *Non-linear multi-scale image registration and segmentation of individual brain structures from MRI Proceedings of IEEE Symposium on Advanced Medical Image Processing in Medicine*: 105-110 ; 1992b
- [ 3 ] Collins D.L., Neelin P., Peter T.M., Evans A.C. *Automatic 3D registration of MR volumetric data in standardized talairach space J Comp Assist Tomogr (in press)*
- [ 4 ] Talairach J. and Tournoux P. *Co-planar stereotaxic atlas of the human brain: 3-Dimensional proportional system: an approach to cerebral imaging Georg Thieme Verlag, Stuttgart, New York* ; 1988
- [ 5 ] Evans A.C., Dai W., Collins L., Neelin P., Marrett S. *Warping of a computerized 3-D atlas to match brain image volumes for quantitative neuroanatomical and functional analysis Proceedings of the International Society of Optical Engineering (SPIE): Medical Imaging V 1445*: 236-247 ; 1991
- [ 6 ] Evans A.C., Marrett S., Neelin P., Collins L., Worsley K., Dai W., Milot S., Meyer E., Bub D. *Anatomical mapping of functional activation in stereotaxic coordinate space NeuroImage 1(1)*: 43-63 ; 1992a
- [ 7 ] Evans A.C., Collins D.L., Milner B. *An MRI-based stereotaxic brain atlas from 300 young normal subjects Proc 22nd Annual Symposium, Society for Neuroscience, Anaheim 179.4* : 408 ; 1992b
- [ 8 ] Kamber M., Collins D.L., Francis G.S., Shinghal R., Evans A.C. *Model-based 3D segmentation of multiple sclerosis lesions in MRI data Visualization in Biomedical Computing, Proc SPIE 1808* : 590-600 ; 1992
- [ 9 ] MacDonald D., Avis D., Evans A.C. *Automatic parameterization of human cortical surfaces Proc Annual Symposium on Information Processing in Medical Imaging (IPMI)* ; 1993